PNAS RESEARCH ARTICLE | APPLIED PHYSICAL SCIENCES

A network model to predict ionic transport in porous materials

Filipe Henrique[a], Paweł J. Żuk[b,c], and Ankur Gupta[a,1]

Edited by Monica Olvera de la Cruz, Northwestern University, Evanston, IL; received January 24, 2024; accepted April 22, 2024

Understanding the dynamics of electric-double-layer (EDL) charging in porous media is essential for advancements in next-generation energy storage devices. Due to the high computational demands of direct numerical simulations and a lack of interfacial boundary conditions for reduced-order models, the current understanding of EDL charging is limited to simple geometries. Here, we present a network model to predict EDL charging in arbitrary networks of long pores in the Debye–Hückel limit without restrictions on EDL thickness and pore radii. We demonstrate that electrolyte transport is described by Kirchhoff's laws in terms of the electrochemical potential of charge (the valence-weighted average of the ion electrochemical potentials) instead of the electric potential. By employing the equivalent circuit representation suggested by these modified Kirchhoff's laws, our methodology accurately captures the spatial and temporal dependencies of charge density and electric potential, matching results obtained from computationally intensive direct numerical simulations. Our network model provides results up to six orders of magnitude faster, enabling the efficient simulation of a triangular lattice of five thousand pores in 6 min. We employ the framework to study the impact of pore connectivity and polydispersity on electrode charging dynamics for pore networks and discuss how these factors affect the time scale, energy density, and power density of capacitive charging. The scalability and versatility of our methodology make it a rational tool for designing 3D-printed electrodes and for interpreting geometric effects on electrode impedance spectroscopy measurements.

porous materials | electrolyte transport | charging dynamics | equivalent circuit | energy storage

Significance

Porous electrodes enhance the capacitance of electrochemical devices by maximizing surface area. However, the relationship between device performance and the porous material structure remains poorly understood. This study introduces a model to predict electrolyte transport in complex networks of slender pores. We derive modified Kirchhoff's laws and equivalent circuit equations for electrolyte transport in charged confinement. Our framework accelerates numerical computations by six orders of magnitude without compromising accuracy. We leverage this model to investigate the influence of connections and pore size distribution on the charging time scale of electrical double layers and predict structure–property relationships. These findings hold potential for improving supercapacitor design and enabling 3D-printed microscale electrodes for wearable energy storage and supercapacitors in Internet-of-Things applications.

Ionic transport in dilute electrolytes has been successfully predicted through the Poisson–Nernst–Planck (PNP) equations and their derivatives (1–5) in simple geometries. Given the central role that ionic transport plays in the porous electrodes of energy storage devices such as electrochemical capacitors and batteries (6, 7), significant effort has been devoted to developing continuum models that describe this phenomenon in confinement (8–11). In these devices, electric double layers store energy through the electrostatic attraction of counterions to the electrode surfaces. Since the capacitance of electric double layers increases with surface area, the electrodes are usually highly porous, consisting of surface areas as high as 3,300 m^2/g (12). One of the exciting developments in the area is the control of porous structures through 3-D printed supercapacitor electrodes, with applications to the Internet of Things (7) and to wearable energy storage (13). However, physical principles of ionic transport and consequently the rational design of pore network geometries with optimal performance remain an open question.

Recent studies have demonstrated that molecular dynamics simulations provide full descriptions of electric-double-layer charging in confinement, including nonidealities due to concentrated electrolytes, high potentials, and surface chemistry (14). Despite these capabilities, their high computational cost precludes the study of large systems with complex pore networks and realistically long time scales (15, 16). Though more computationally favorable than molecular dynamics, modified PNP equations (17–22) and dynamic density functional theory (23, 24) are also challenging to employ in porous media due to the geometrical complexity.

In view of these shortcomings, transmission-line (TL) models stemming from the seminal work of de Levie (25, 26) continue to be used as a good qualitative guide of the physics of electrolyte charging in experimental investigations (27, 28). Their use can be justified by similar diffusion-like equations found in more detailed dynamic density functional theory models (14) and good matches obtained with experimental results using fitting parameters (16, 29, 30).

Nevertheless, the majority of the TL models are conceived as single-pore models. de Levie's model, for instance, may be formally justified by a linearization of the PNP equations for a single pore at low electric potentials (16) in the thin-double-layer limit (31). Variations of the TL model account for high potentials (9), surface conduction

Author contributions: F.H., P.J.Ż., and A.G. designed research; F.H., P.J.Ż., and A.G. performed research; F.H. and A.G. analyzed data; and F.H., P.J.Ż., and A.G. wrote the paper.

The authors declare no competing interest.

This article is a PNAS Direct Submission.

[1]To whom correspondence may be addressed. Email: ankur.gupta@colorado.edu.

This article contains supporting information online at https://www.pnas.org/lookup/suppl/doi:10.1073/pnas.2401656121/-/DCSupplemental.

Published May 24, 2024.

(10), arbitrary double-layer thickness (32, 33), ionic diffusivity asymmetry (34), or a stack-electrode model (35). However, none of these variations capture the geometric effect of pore connections or pore sizes beyond a lumped-parameter approach.

In our view, this crucial knowledge gap exists because of two primary reasons. First, the direct numerical simulation of PNP in an arbitrary network of pores is computationally infeasible. Second, while it is understood that the dynamics of double-layer charging in single pores differs between the thin- and the overlapping-double-layer limits (32, 33), the interaction of pores of different sizes remains undescribed.

In this article, we devise a comprehensive network model to predict the electric-double-layer charging of a binary electrolyte in arbitrary networks of long pores in the Debye–Hückel limit. The proposed approach provides reduced-order transport equations in each pore and describes voltage and charge relationships across junctions and loops of pores, i.e., effective Kirchhoff's laws for electrolyte transport in porous media that close the system of equations. We emphasize that these modified Kirchhoff's laws are required to capture the simultaneous effects of diffusion and electromigration, whereas the original Kirchhoff's laws of TL circuits are only valid for purely electromigrative transport. These effective Kirchhoff's laws are written for the electrochemical potential of charge, i.e., for the valence-weighted average of the ion electrochemical potentials, instead of the electric potential. We compare our approach against direct numerical simulations of the PNP equations for a range of different geometries and demonstrate that our approach is able to recover the spatial and temporal dependencies of charge density and electric potential. The TL model devised is computationally inexpensive and enables the simulation of a triangular network consisting of ~5,000 pores in 6 min (Fig. 3), whereas our direct numerical simulations of the full PNP equations take upward of a month for a 3-pore network using 28 cores (*Materials and Methods*). The scalability of the proposed TL methodology enables us to quantify the impact of pore size distribution and pore connectivity, and consequently to uncover guiding principles for optimizing the design of porous electrodes.

Results and Discussion

Charging Dynamics. Throughout the article, we represent dimensionless variables by asterisks to distinguish them from their dimensional counterparts. We consider a network of N long cylindrical pores within a perfectly conducting and ideally blocking electrode at a potential ϕ_D relative to an ion reservoir. Supercapacitor electrode materials are typically highly conductive (6). However, a finite electrode conductivity could be incorporated through Ohm's law for the solid phase (36–38). The reservoir is connected to the inlet pores through static diffusion layers, as illustrated in Fig. 1*A*. The pore network is arbitrary, allowing us to study the effects of pore size distribution, connectivity, and spatial arrangement. We assume that the porous network is filled with a binary and symmetric electrolyte with ion diffusivity D, though it is straightforward to extend this work to asymmetric ion diffusivities and valences (34). We neglect convection in the species transport equations. In the Debye–Hückel regime, where the applied potential is low compared to the thermal voltage kT/e, i.e., $\epsilon = \phi_D e/(kT) \ll 1$, this approach is justifiable since electroosmotic flows are $O(\epsilon^2)$, whereas diffusive and electromigrative fluxes are $O(\epsilon)$. We note that electroosmotic flow loops in porous media can affect charge transport for applied potentials above ~0.4 V (39).

In our model, variables indexed by i pertain to the i-th pore, with dimensionless radial and axial coordinates $r_i \in [0, a_i]$ and $z_i \in [0, \ell_i]$. $a_i/\ell \ll 1$ is the long-pore requirement, where ℓ is the average pore length. The reservoir concentration c_∞ of either ionic species is taken as the concentration scale, thus the Debye length takes the form $\lambda_D = \sqrt{\varepsilon kT/(2e^2 c_\infty)}$ where ε is the electrolyte permittivity. The key question that we seek to address is how pores of different sizes interact to collectively encode an effective charging time scale in the network. To answer this question, we derive a TL model from the PNP equations. A brief presentation of the derivation is given in the main text along with the physical interpretation of the results of the model and the definitions of the variables. Additional details of steps of the derivation of the governing equation and initial and boundary conditions can be found in *SI Appendix*.

In the Debye–Hückel regime, the charge density ρ is produced by gradients of the electrochemical potentials of the ions according to

$$\frac{\partial \rho}{\partial t} = \frac{D\varepsilon}{\lambda_D^2}\nabla^2\left(\frac{\mu_+ - \mu_-}{2e}\right) \quad [1a]$$

and

$$-\varepsilon\nabla^2\phi = \rho = e(c_+ - c_-), \quad [1b]$$

where t is time, $\mu_\pm$ are the electrochemical potentials of cation and anion, respectively, $c_\pm$ are their concentrations, and ϕ is the electric potential. For dilute electrolytes, the electrochemical potentials of the ions take the forms $\mu_\pm = kT\ln c_\pm \pm e\phi$. Due to its role as the effective potential for charge transport, we define the electrochemical potential of charge $\varphi = (\mu_+ - \mu_-)/(2e)$, where the dimensions of φ are purposefully kept the same as those of the electric potential ϕ to allow for direct comparisons between the two when deriving effective Kirchhoff's laws. As the prefactor of the Laplacian of the effective electrochemical potential, $\sigma = D\varepsilon/\lambda_D^2$ can be interpreted as a conductivity. In the low-applied-potential limit, φ takes the asymptotic form

$$\varphi = \phi + \frac{\lambda_D^2}{\varepsilon}\rho. \quad [2]$$

The prefactor λ_D^2/ε can be interpreted as the required unit conversion from charge density to electric potential, as seen from Poisson's equation Eq. **1b**. The long-pore condition allows us to invoke radial equilibrium (i.e., no radial flux) at each time to impose the radial homogeneity of φ, thus constraining the radial dependencies of the charge density ρ_i and the potential ϕ_i by the relation

$$\varphi_i(z_i, t) = \phi_i(r_i, z_i, t) + \frac{\lambda_D^2}{\varepsilon}\rho_i(r_i, z_i, t). \quad [3]$$

Eq. **3** could also be understood as a Boltzmann distribution in the radial direction, linearized for low potentials. The axial charge flux averaged over a cross-section is proportional to $-\frac{\partial}{\partial z_i}\left(\bar{\phi}_i + \varepsilon\bar{\rho}_i/\lambda_D^2\right)$, where bars represent the averages. The derivatives of the averages of electric potential and charge density describe the electromigrative and diffusive flux, respectively.

We perform an order-of-magnitude analysis to estimate the contributions of these fluxes for pores of different sizes. In the thin-double-layer limit, $a_i \gg \lambda_D$. Assuming that the electric potential is of the order of the applied potential over formed double layers and drops to zero in the electroneutral bulk, it follows from Eq. **3** that the average charge density is given by

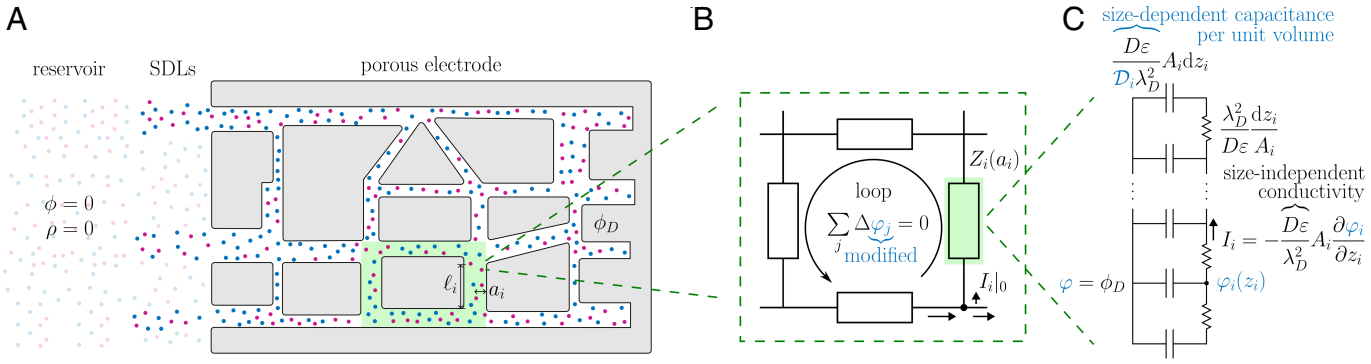

Fig. 1. TL model for electric-double-layer charging in networks of long pores. (*A*) Schematic of an arbitrary porous electrode geometry representable by a network of long pores, with cations in purple and anions in blue. The electroneutral reservoir (transparent ions) has a reference potential $\phi = 0$, connected through static diffusion layers (SDLs) (opaque ions outside the electrode) to the inlet pores. The perfectly conducting electrode is at a potential ϕ_D. The pores can be cylinders or slits. The length, radius, and area of the i-th pore are, respectively, ℓ_i, a_i, and A_i. (*B*) EDL charging in a group of pores represented by a circuit loop. The balance of diffusion and electromigration requires effective forms of Kirchhoff's laws written in terms of the electrochemical potential of charge $\varphi_i = \phi_i + \lambda_D^2\rho_i/\varepsilon$ of each pore, which is continuous across junctions as seen from Eq. **5b**. The impedance of each pore is written as $Z_i(a_i)$ and the current at $z_i = 0$ by $I_i|_0$. Features that differ from de Levie's circuit in parts *B* and *C* are represented in light blue. (*C*) Transmission-line representation of EDL charging in each pore of the network for arbitrary Debye lengths. The pore-size-dependent impedance is consistent with ref. 33 for an isolated pore. From Eq. **1a**, each resistor has the same conductivity $D\varepsilon/\lambda_D^2$ and from Eq. **4**, each capacitor has a capacitance per unit volume $D\varepsilon/(\mathcal{D}_i\lambda_D^2)$.

$\bar{\rho}_i/(\varepsilon/\lambda_D^2) \sim \lambda_D\phi_D/a_i \ll \phi_D$ for thin double layers in charged regions. Due to a low contrast to the uncharged regions, the diffusive charge flux can therefore be neglected. The thin-double-layer limit thus greatly simplifies the analysis and has been widely explored in the literature (9, 10, 25, 26, 40). For an arbitrary a_i, however, one cannot further simplify the axial flux as both diffusion and electromigration could be important.

The relative importance of electromigration and diffusion could change across a junction, depending on the radii of the connected pores. As an example, let us consider a simple scenario with only two pores connected by a junction: one pore has a radius in the thin-double-layer limit such that $a_i \gg \lambda_D$, and the other pore has a radius in the overlapping-double-layer limit such that $a_j \ll \lambda_D$. For the pore with a thin double layer, as the charge density and the potential screening are restricted to the double layer, the argument of the previous paragraph holds, such that $\bar{\phi}_i \sim \lambda_D\phi_D/a_i \ll \phi_D$ and $\bar{\rho}_i\lambda_D^2/\varepsilon \sim \lambda_D\phi_D/a_i \ll \phi_D$. However, for the pore with an overlapping double layer, as charges are present throughout the cross-section and not fully screened, electric potentials are of order ϕ_D throughout the cross-section, implying $\bar{\phi}_j \sim \phi_D$ and consequently $\bar{\rho}_j\lambda_D^2/\varepsilon \sim \phi_D$. As evident from the above discussion, the steady-state charge and potential distributions in the pores will be different. Therefore, the junction will present sharp changes in potential and charge to adhere to the individual behavior of the pores (32–34). The preceding discussion focuses on two pores, but in reality, there could be a large number of connected pores and multiple junctions, which could further complicate the analysis.

The complexity of the charge and electric potential profiles across junctions is reduced by the usage of the electrochemical potential of charge to represent charge transport. φ_i does not vary along a cross-section—Eq. **3**—or across a junction due to flux matching across short connections compared to the pore lengths. Physically, the continuity of the electrochemical potential of charge across junctions is similar to the continuity of electric potential across a node of an electric circuit (41), of temperature across an interface (42), or of electrochemical potentials across a liquid junction (43). In summary, while $\bar{\phi}_i$ and $\bar{\rho}_i$ could present sharp changes across a junction, φ_i is continuous throughout the region. As such, φ_i is a natural quantity to describe the transport of a symmetric electrolyte inside a porous network.

The usage of φ_i simplifies the description of double-layer charging in a porous network in two primary ways. First, the total axial charge flux is given by $-\frac{D\varepsilon}{\lambda_D^2}\frac{\partial\varphi_i}{\partial z_i}$ and thus the conductivity of all pores is equal. We underscore that this would not be true if we had defined conductivity based on electric potential, as the conductivity would need to be adjusted depending on a_i. Second, since φ_i is continuous across a junction, it can be used in TL circuit representations without introducing circuit elements to represent the junctions. On the other hand, $\bar{\phi}_i$ would be modeled as discontinuous since it can change across junctions due to different extents of double-layer screening as a function of a_i. Though ionic electrochemical potentials have been used as the thermodynamic force driving electroosmotic flow in confinement (44, 45), the continuity of the effective electrochemical potential of charge in porous media had not been leveraged in TL representations of double-layer charging.

Before presenting the junction boundary conditions, we briefly describe the transport equations for each pore. Solving Eq. **1b** asymptotically for the dominant radial dependency and using this result to average Eq. **1a** over a cross-section with no-flux boundary conditions,

$$\frac{\partial\varphi_i}{\partial t} = \mathcal{D}_i\frac{\partial^2\varphi_i}{\partial z_i^2}, \qquad [4]$$

where $\mathcal{D}_i = Da_iI_0(a_i/\lambda_D)/(2\lambda_DI_1(a_i/\lambda_D))$ is the effective charge diffusivity in the i-th cylindrical pore and I_n is the modified Bessel function of the first kind of order n. For $a_i \gg \lambda_D$, i.e., the thin-double-layer regime, $\mathcal{D}_i \sim Da_i/(2\lambda_D)$ and the diffusion coefficient is set by electromigration alone. For the overlapping double layer regime, where $a_i \ll \lambda_D$ and $\mathcal{D}_i \sim D$, the diffusion coefficient is set by diffusion alone. For moderate a_i/λ_D, the diffusion coefficient is set by a balance of electromigration and diffusion.

We stress that $\mathcal{D}_i$ is different in different pores. By controlling the rate of charge transport (or equivalently the ratio of the electrochemical potential of charge that is converted into average charge density of a cross-section), $\mathcal{D}_i$ sets the rate of local charge accumulation, such that it is inversely proportional to the pore capacitance per unit volume $D\varepsilon/(\mathcal{D}_i\lambda_D^2)$; see Fig. 1*C*.

The relationship described in Eq. **4** for arbitrary a_i was first recognized in our work for a single pore (33), where it was reported in terms of the average electric potential.

Eq. **4** is a TL equation, but a circuit interpretation also requires that the boundary conditions be such that Kirchhoff's laws hold. Therefore, we now focus on the junction boundary conditions, which are a crucial element of this work. We write current conservation across each junction as

$$\sum_{i\in\text{junction}} A_i\hat{\mathbf{n}}_i\cdot\nabla_i\varphi_i|_{z_i(\text{junction})}=0, \qquad \textbf{[5a]}$$

where A_i is the cross-sectional area of a pore, $\hat{\mathbf{n}}_i$ is the unit normal vector to A_i pointing away from the junction volume, and the sum is effected over all the pores connected to the junction.

Physically, Eq. **5a** is essentially Kirchhoff's current law for the identical conductivities of the electrochemical potentials of charge of all pores. However, Eq. **5a** only provides a single equation relating the potentials φ_i across a junction. The next set of equations states the continuity of the electrochemical potential of charge across any junction:

$$\varphi_i|_{z_i(\text{junction})}=\varphi_j\big|_{z_j(\text{junction})},\ (i,j)\in\text{junction}, \qquad \textbf{[5b]}$$

where i and j are any distinct pores connected to a junction, while z_i(junction) and z_j(junction) are the axial coordinates of the points where their centerlines intersect the junction; see Fig. 2*A*. This boundary condition is equivalent to the continuity of voltage across nodes of electrical circuits. We reiterate that, for confined electrolytes, Eq. **5b** cannot be written for the average electric potentials since $\bar{\phi}_i$ could experience a sharp change across a junction. For a circuit represented in terms of φ_i, Eq. **5b** enables one to write that the drop of electrochemical potentials of charge across a loop of pores is zero, i.e., $\sum_{i\in\text{loop}}\Delta\varphi_i=0$ where $\Delta\varphi_i=\varphi_i(z_i=\ell_i)-\varphi_i(z_i=0)$, or a modified Kirchhoff's voltage law. As such, Eq. **5** represent a set of modified Kirchhoff's laws in terms of φ_i, which enable us to close the system of equations in an arbitrary network of pores; see Fig. 1 *B* and *C*. We highlight that φ_i provides the ability to capture both electromigrative and diffusive fluxes in the system and thus expands the ability to study ionic transport in confined geometries.

We note that to solve Eq. **4** in each pore, in addition to Eq. **5** as boundary conditions across junctions, we also need initial conditions as well as the boundary conditions at the SDL/pore interfaces and pore dead ends. These conditions are straightforward and are omitted here for brevity; they are listed in the *Materials and Methods* and systematically deduced in *SI Appendix*.

Validation. To probe the accuracy of the proposed asymptotic model, we perform direct numerical simulations (DNS) of the full PNP equations for a simple geometry—the Y-junction shown in Fig. 2*A*. There, an inlet slit pore is connected on one end

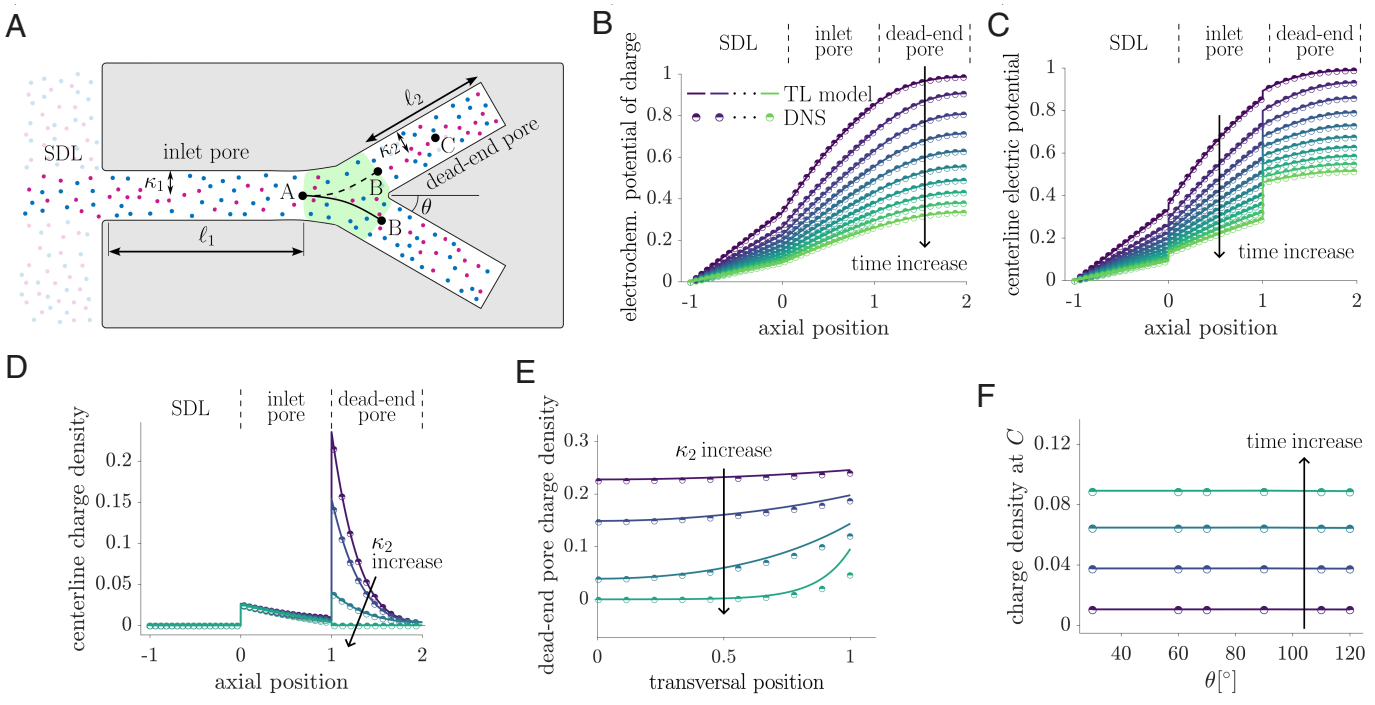

Fig. 2. Validation of the TL model for a Y-junction of slit pores. Dimensionless properties are defined by $y_i^*=y_i/h_i$, $z_i^*=z_i/\ell$, $t^*=t/(\ell^2/D)$, $\phi_i^*=\phi_i/\phi_D$, $\rho_i^*=\rho_i/(\epsilon\phi_D/\lambda_D^2)$, and $\varphi_i^*=(\mu_+-\mu_-)/(2e\phi_D)$. (*A*) Schematic of the Y-junction geometry of slit pores used for the comparison of the TL model with DNS. The junction is shown in green. (*B*) Electrochemical potential of charge φ_i^* and (*C*) Centerline electric potential $\phi_i^*(y_i^*=0)$ vs. axial positions z_i^* along the pores and the SDL for ten equally spaced times t^* in the interval [0.008, 0.098], with $\kappa_2=2$. TL analytical results (*SI Appendix*) represented by solid lines and DNS results by half-filled orbs for all plots in parts *B*–*F*. The use of effective Kirchhoff's laws for the junction gives accurate results in the pore domains up to a distance on the order of the largest radius away from the intersection of the centerlines. Good matching with the DNS is observed for all the times examined. (*D*) Centerline charge density vs. axial position along the pores and the SDL and (*E*) Dead-end pore charge density at $z_2^*=0.1$, $\rho_2^*(z_2^*=0.1)$ vs. transversal coordinate y_2^*, both for all dead-end pore relative sizes $\kappa_2\in\{0.4, 0.8, 2, 8\}$. The TL model presents good agreement with DNS even at $z_2^*=0.1$, approximately 100 nm from the transition region. For higher pore sizes, with larger junction widths, some disagreement may be found in the double layers close to the junction. (*F*) Charge density at the centerline midpoint *C* of the dead-end pore, $\rho_2^*(y_2^*=0, z_2^*=0.5, t^*)$, vs. the half-angle between the centerlines of the dead-end pores, θ, for four equally spaced times $t^*\in[0.01, 0.04]$. The TL model predictions of continuity of φ and independence of all variables on θ for long pores are supported by the DNS.

to the reservoir through an SDL and on the other end to two identical dead-end slit pores. We note that slits were adopted to facilitate the DNS; *SI Appendix* shows that the only change required in the model to capture this geometry is in the effective diffusivity function, given by $\mathcal{D}(\kappa_i) = D\kappa_i \coth(\kappa_i)$ for slits, where the relative size of the i-th pore, κ_i, is given in terms of its half-width, h_i, by $\kappa_i = h_i/\lambda_D$. Fig. 2 *B* and *C* compare the dimensionless electrochemical potential of charge $\varphi_i^*(z_i^*, t^*)$ and centerline potential $\phi_i^*(y_i^* = 0, z_i^*, t^*)$ as predicted by the TL model and the DNS. We note that there is an excellent agreement for both the early and late dynamics. Fig. 2 *B* and *C* demonstrate that while φ_i^* is continuous across the SDL/pore interface as well as the junction, the centerline electric potential has sharp changes; see also insets of zoom-ins of these results in *SI Appendix*. Note that these sharp changes are also present at steady-state since double layers are screened to different extents according to the relative pore sizes.

We compare the charge profiles in Fig. 2 *D–F*. Fig. 2*D* shows that the theory predicts the centerline charge density profile adequately from $\kappa_2 = 0.4$ to $\kappa_2 = 8$, a range that extends from the overlapping- to the thin-double-layer limit. We find a very good agreement between the proposed model and the DNS. To further understand the dependency of the matching on the junction characteristics, we show the dead-end pore charge profile vs. the transversal coordinate y_2^* in Fig. 2*E* at $z_2^* = 0.1$, dimensionally 100 nm away from the intersection of centerlines of the inlet and dead-end pores. We note that there is good agreement between the theoretical profiles and DNS for moderately to highly overlapping double layers. For larger dead-end pore sizes, the length scale of the influence of the junction region on the charging profile becomes more pronounced, such that a slight quantitative disagreement is noticed in the thin double layers.

A key inference of the proposed model is the independence of the charge and potential profiles on the angles between long pores in a junction. In fact, in the assumed asymptotic regime of slender pores, transport becomes one-dimensional and the split of current at any junction becomes only a function of the two properties: the number of connected pores and their radii, as seen from Kirchhoff's current law—Eq. **5a**. We test this hypothesis by comparing the time evolution of the charge density at the midpoint of the centerlines of both dead-end pores for multiple angles between these centerlines. Fig. 2*F* shows that, as predicted by the model, the charge profile is roughly independent of this angle over time. This result is valid across a wide range of angles, from $2\theta = 60°$ to $240°$. It implies that our results should hold for pore connections in three-dimensional networks, provided the pores are slender.

The above analysis demonstrates that the proposed approach based on effective Kirchhoff's laws in terms of φ_i is able to recover all the crucial features of the double-layer charging in the Y-junction. We reiterate that this approach applies to arbitrary networks of long pores and does not require that the electric double layers be thin or that the porous structure be periodic, and it is computationally affordable. In fact, while the DNS of the Y-shaped junction takes 4 million seconds for each second elapsed in the simulation (*Materials and Methods*), a numerical solution of the TL equations takes under a second, i.e., it is up to six orders of magnitude faster than the DNS and thus is highly scalable. In the remainder of the article, we focus on the insights of the model on pore connectivity and spatial arrangement effects. To this end, we undertake case studies of simple lattice geometries, though the model can be applied to arbitrary three-dimensional networks of slender pores.

Effects of the Spatial Arrangement of Pores. A limitation of the existing theoretical frameworks for EDL charging in porous media, such as porous-electrode theories (9, 10, 46) and stack- (35) and laminate-electrode (47) theories, is the inability to resolve microstructural features of arbitrary porous structures, such as coordination numbers and distinct arrangements of pore sizes. To illustrate the application of the current TL model to the study of such effects, we first consider the porous network shown in Fig. 3*A*. Counterions are transported from the reservoir into the pores through the SDLs. The network consists of a 4×5 array of nodes, representing electrode inlets, junctions, or pore dead ends. These nodes may be connected by horizontal or vertical pores, represented by light yellow rectangles. To focus on the characterization of distinct configurations at the microscale, we compare structures with the same number of pores, but in different positions of the lattice. We fix 12 horizontal pores connecting the first three columns of all four rows and let an arbitrary number X of pores be moved. They may be placed in any of the positions outlined by dashed lines in Fig. 3*A*. The rules of pore placement resemble a matchsticks puzzle, but the question here is "What spatial arrangement of pores achieves the lowest charging time scale?"

For each number of movable pores, X, there is at least one configuration with a minimal charging time scale. These minimal charging time scales (normalized by the distance between the vertical endpoints of the lattice to allow for comparisons between lattices of different lengths) are plotted as a function of the number of movable pores in Fig. 3*B*, along with the optimal configurations. We see that the strategy for achieving optimal charging consists in placing the mobile pores close to the reservoir, such that the length traversed by the ions to reach their equilibrium positions is reduced. In fact, Fig. 3*C* shows that moving vertical connections away from the reservoir does not affect the early stage of the charging process, but it decelerates the late-time dynamics. Perhaps surprisingly, placing the mobile pores near the reservoir is the optimal strategy despite causing early divisions of the current at the vertical connections. Another available option would be to place the mobile pores horizontally after the fixed pores, making an effectively longer capillary bundle, but it also turns out to be suboptimal since the time scale increases quadratically with pore length, but only linearly with divisions of current; a detailed discussion of this phenomenon can be found in *SI Appendix*.

In Fig. 3 *D* and *E*, we show that we can also simulate larger and more complex networks with the TL model; see also Movie S1. They display square domains with 30 inlets and triangular lattices where the slanted pores are added pseudorandomly. For each location, the placement of a slanted pore is decided based on the value of a pseudorandom number drawn from the uniform distribution. If the random number is greater than a threshold, the pore is added. Fig. 3*E* shows the network when all 4,988 pores are present. In this case, the equations are solved in 6 min; see *Materials and Methods* for our computational methodology. For each probabilities of acceptance shown in Fig. 3*F*, the charge evolution is exponential at long times, with a single time constant. As in Fig. 3*B*, the inclusion of additional pores alters the time scale of relaxation to steady-state.

Combined Effects of Polydispersity and Spatial Arrangement. The analysis in the prior section highlights the sensitive dependency of the net charging time scale on the arrangement of the pores. However, the literature primarily uses the pore size distribution to characterize the electrode structure (48, 49). This invites the following question: given the polydispersity of

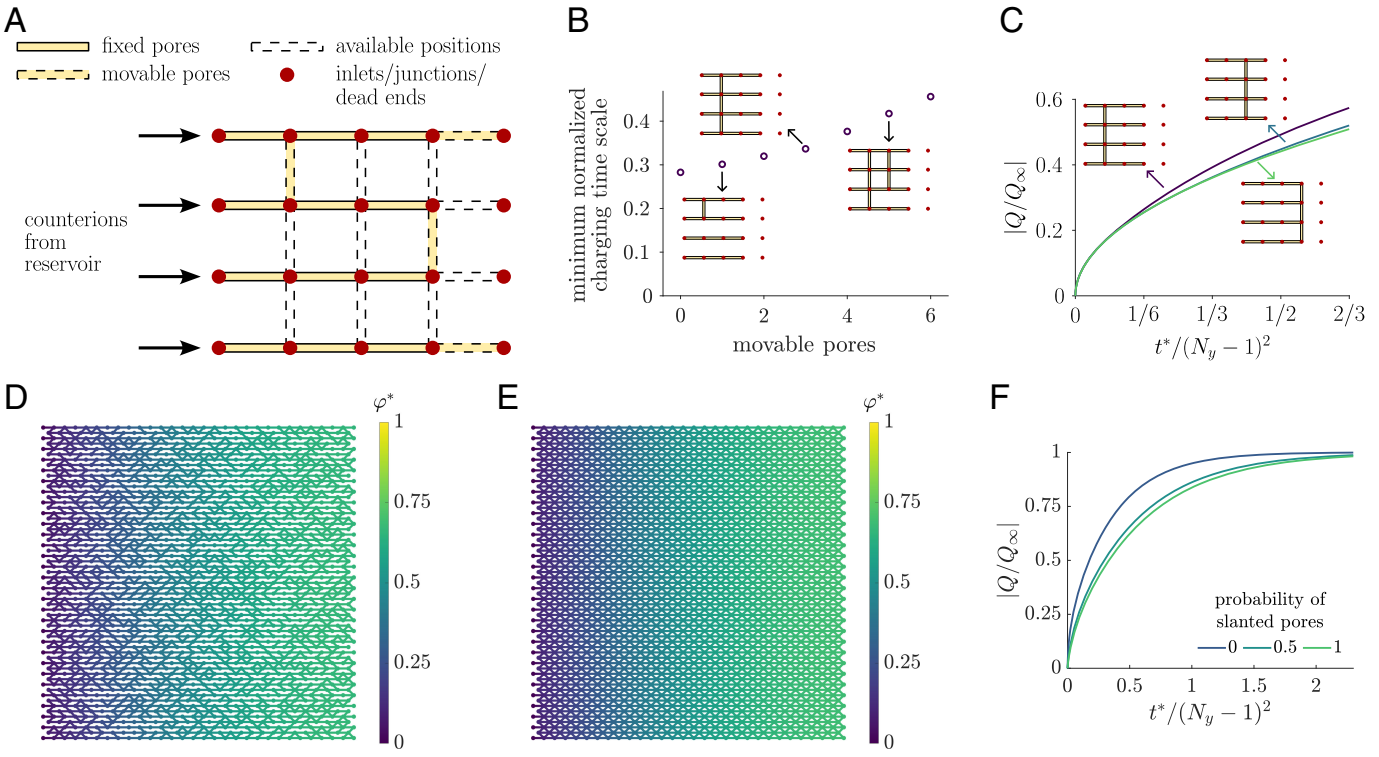

Fig. 3. Effects of spatial arrangement on the charging time scale of lattices. Times are normalized by a scale of diffusion $\ell^2(N_y-1)^2/D$ based on the height of the lattice, where N_y is the number of inlets. The network charge is normalized by its steady-state limit Q_∞. (*A*) Schematic of the possible pore arrangements on the 4×5 lattice. Pores are shown as light yellow rectangles; inlets, junctions, and dead ends are shown as red circles. Counterions are transported from the reservoir into the pores. The 12 horizontal pores outlined by solid lines, which connect the first three columns of each row, are fixed. *X* pores are movable; they may be placed in any of the positions outlined by the dashed rectangles. (*B*) Normalized minimal charging time scale of all possible configurations vs. the number of movable pores. Optimal configurations are achieved by placing the pores as close to the reservoir as possible. (*C*) Normalized lattice charge vs. normalized time for the configurations shown in the plot, with $X = 3$. The smaller distances traversed by ions in pores close to the reservoir optimize late-time charging. Early-time charging is not influenced by these arrangements. (*D* and *E*) Triangular lattices with 30 inlets in a square domain, with slanted-pore acceptance probabilities of 0.5 (*D*) and 1 (*E*). (*F*) Normalized lattice charge for different acceptance probabilities of the slanted pores. An increasing porosity slows down the long-time exponential charging.

a pore network, how sensitive is its charging time scale to the arrangement of the pores?

To address this question, we consider 8×8 fully connected pore lattices with pore sizes sampled from log-normal distributions with different polydispersities and arrange them in three different configurations. The first one, which we refer to as converging, is shown in Fig. 4*A*. In this case, the horizontal and vertical pore sizes both decrease in the direction of charging. A second one, "random," is realized when the placement of pores is determined randomly by the order in which their sizes are drawn. The last one, diverging, shown in Fig. 4*B*, has increasing pore sizes in the direction of charging. The top and bottom halves of the lattices in Fig. 4 *A* and *B* show, respectively, the contours of the electrochemical potential of charge and the electric potential at a given time. As shown in the zoomed-in pores of Fig. 4*A*, the electrochemical potential of charge is predicted to be constant across the junctions, whereas the electric potential changes across junctions to reflect the contrast in steady-state profiles arising from the different extents of electric field screening in pores of unequal sizes. In the zoomed-in junction, the contours of the narrowest pore have a lighter purple color, indicating the smaller extent of double-layer screening.

Qualitatively, Fig. 4 *A* and *B* show that the profiles of the converging and diverging arrangements of the pores are different, even if the polydispersity is identical. Specifically, we observe that the converging arrangement charges faster, as further shown in Movies S2 and S3. In the converging scenario, the relative pore sizes κ_i are larger near the reservoir, which causes the effective diffusion coefficients $\mathcal{D}_i$ to be larger as they are dominated by electromigration. In contrast, in the diverging scenario, the narrow inlet pores are bottlenecks; their $\mathcal{D}_i$ are smaller since they are diffusion-dominated. Recent molecular dynamics results have reported a similar strategy of a converging cross-section of a nanometer-wide pore for ion transport optimization (50)—though at this length scale, it is a result of the reduction of steric hindrance of co-ion desorption, not addressed in this work.

Quantitatively, the charging time scale and power density (Eqs. **12** and **13**) for all the configurations are shown in Fig. 4 *C* and *D*. We find that for higher polydispersities, the difference between the three configurations becomes more pronounced. For a moderate polydispersity of 0.17, the relative pore sizes of the largest and smallest horizontal pores were 2.35 and 1.18, differing by a factor of two. In this case, the charging time scales of the converging and diverging time scales differ by a factor of 2.2. Even when compared to the random lattice, the converging configuration showed a power density 1.3 times higher. Interestingly, higher polydispersity may be even desirable for the converging scenario since inlet pores significantly influence the charging time scale. However, such a preference is only likely to hold for a low porosity system since volume constraints, which are currently not accounted for in the aforementioned results, will start to impact the analysis.

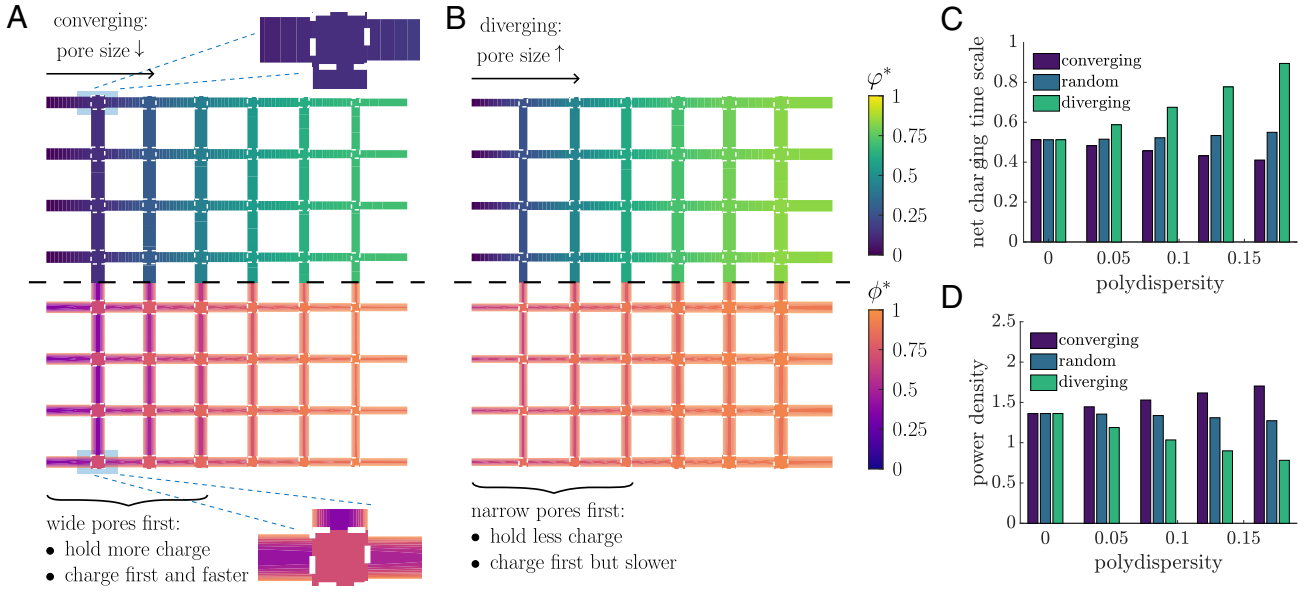

Fig. 4. Effects of polydispersity and configuration in the charging characteristics of lattices. (*A* and *B*) Contour plots of charge density in 8 × 8 fully connected pore network lattices with different arrangements of a set of relative pore sizes drawn from a log-normal distribution with average relative pore size $\langle\kappa\rangle = 2$ and polydispersity $= \langle\kappa\rangle/\mathrm{sd}(\kappa) = 0.17$. Pore sizes are (*A*) decreasing ("converging") and (*B*) increasing ("diverging") in the direction of charging. *Insets* of two junctions of pores in equivalent positions are indicated by the light blue transparent boxes and dashed lines. (*C*) Lattice net charging time scale, i.e., the time required to reach 70.18% of steady-state charge, and (*D*) lattice power density (Eqs. **12** and **13**) vs. polydispersity for converging, random, and diverging orders of pore sizes in the direction of charging. The importance of the pore size arrangement increases with the polydispersity. For converging configurations, the largest pores are near the reservoir. Their effective screening of the electric potential boosts electromigration, promoting faster charging. Since they hold the highest fractions of charge and are charged first, the net charging time scale decreases. On the other hand, in a diverging configuration, the diffusion-dominated transport in the inlet pores is a bottleneck. While it does not affect the capacitance, the power density decreases by a factor of 2.2 compared to the previous case.

Crucially, our results highlight that polydispersity alone is not sufficient to understand the charging and discharging dynamics of an electrode, and more consideration should be given to parameters describing the connectivity and spatial arrangement of pores. These particular effects and analyses are made possible due to the network model developed in this manuscript and, as such, had not been explored in prior literature.

Conclusions

We propose a model for the electric-double-layer charging in arbitrary networks of long pores which demonstrates effective Kirchhoff's laws based on the electrochemical potential of charge, defined here as the valence-weighted average of the ion electrochemical potentials $\varphi = (\mu_+ - \mu_-)/(2e)$. The proposed methodology is able to recover the spatial and temporal dependencies of charge density and electric potential obtained from direct numerical simulations but with a speed that is up to six orders of magnitude faster. We briefly discuss the implications of the model on the effects of pore arrangement and polydispersity and uncover the interplay of these factors on the dynamics of electrode charging for idealized pore networks.

Our work has broad implications for the characterization of ionic transport in porous media. For instance, it provides a framework to explore the impact of pore network morphology through connectivity, tortuosity, and polydispersity simultaneously to connect the microstructure to macroscopic properties, which is a crucial knowledge gap in the literature (35, 51). One of the promising avenues of our work is its impact on electrode impedance spectroscopy (EIS) and mapping out effective circuits for different porous networks. The electrochemical experiments rely significantly on EIS but do not currently have a methodology to map out the impact of connectivity, apart from the single-pore TL models. As an example, one can take a 3D microstructure of an electrode, convert it into a ball-stick model, and employ our methodology to forecast Nyquist plots of impedance. Since we do not apply restrictions on double-layer thickness, this can provide insights into the charging dynamics that were not possible previously.

The work also opens up opportunities for incorporating the effects of the geometry of the pores and other interaction potentials, which have been argued to be important under confinement, or concentrated solutions, where ionic correlations (52) and steric hindrance (17) may become important. While the analysis above is limited to the classical treatment of linearized Poisson–Boltzmann systems, our framework is general and the idea of employing the equality of the electrochemical potential of charge to evaluate electric potential jumps across a junction could be extended to include other interaction parameters. Other effects such as diffusivity contrast (34), mixtures of electrolytes (52, 53), and surface reactions (40, 53, 54) are also possible to incorporate.

From a practical standpoint, the framework presents a rational methodology to design 3D-printed electrodes (55), which are gaining traction in the literature, especially for low-tortuosity materials. The analysis of charging dynamics for a given 3D-printed electrode structure could be carried out through this approach and it could thus guide the design of electrodes. Additionally, there is a growing interest in developing electrodes with pseudocapacitive materials, where there is an interplay of EDL charging in porous media and surface reactions, which our methodology can handle by changing the ideally blocking electrode condition to a reactive flux condition (6, 7, 53, 54). Such a complete continuum model of pseudocapacitive charging of porous media would be fundamental as a basis with which to compare results of experiments and molecular dynamics simulations (56), allowing studies to parse apart intrinsically molecular effects from the predictions of a classical Debye–Hückel theory for reactive porous media.

Relevant theoretical challenges to potential extensions of the current framework to wider use cases relate to its reliance on small applied potentials. While this limit is experimentally relevant to EIS, applied potentials above ~ 0.4 V may introduce a significant spatial dependency of the conductivities of the pores, hindering equivalent circuit representations. Furthermore, applied potentials on that scale drive electroosmotic flow loops in porous media (39), which can affect the EDL charging dynamics. However, we hope the current work will motivate extensions to moderate potentials based upon long-pore asymptotics of the PNP equations and radial quasi-equilibrium for moderate applied potentials supplemented by suitable junction boundary conditions.

Materials and Methods

Direct Numerical Simulations. The nonlinear PNP equations for binary symmetric electrolytes are (42)

$$\frac{\partial c_\pm}{\partial t} = D\left[\nabla^2 c_\pm \pm \frac{e}{kT}\nabla\cdot(c_\pm\nabla\phi)\right] = -\nabla\cdot\mathbf{N}_\pm, \qquad [6a]$$

where $\mathbf{N}_\pm$ are the dimensional ionic fluxes, and

$$-\varepsilon\nabla^2\phi = e(c_+ - c_-). \qquad [6b]$$

These equations were solved numerically by direct numerical simulations for the Cartesian Y-junction geometry illustrated in Fig. 2*A*. As illustrated in *SI Appendix*, only the bottom half of the domain is represented in the simulations due to top–down symmetry about the collinear centerlines of the SDL and the inlet pore. The domain consists of the SDL, with a centerline of length $\ell_s = 1$ μm and a half-width of 76 nm, decreased by a circular fillet of radius 38 nm at the connection to the inlet pore, of length $\ell_1 = 1$ μm and half-width 38 nm. The end of the inlet pore is then connected to a dead-end pore of centerline length $\ell_2 = 1$ μm and variable half-width; see Fig. 2 *D* and *E*. This junction has a fillet of an eighth of a circle of radius 38 nm at its right side. We describe the domains of application of the initial and boundary conditions in the terms indicated in *SI Appendix*.

The finite-volume method (57, 58) was employed for the solution using the open-source software OpenFOAM (59, 60). To this end, first Eq. **6b** alone was run under electroneutral conditions to set up the electric field in the SDL, producing the initial conditions: ϕ a solution of

$$\nabla^2\phi = 0 \qquad [7a]$$

and

$$c_\pm = c_\infty \qquad [7b]$$

in the entire electrolyte domain. The boundary conditions are the same as in the previous work of Gupta et al. for a single pore (32). They are summarized in Table 1. The numerical solution of Eq. **7** for the initial conditions and Eq. **6** with the boundary conditions in Table 1 for the time evolution was performed using a 28-core workstation made available by the Princeton Research Computing resources. It had a computational cost of 4 million seconds for each second elapsed in the simulation.

Numerical Solution of the Transmission-Line Model. The dimensionless form of the transmission-line equation, Eq. **4**, is supplemented by the boundary conditions in Eq. **5** and the initial condition of unscreened potential,

$$\varphi_i(z_i, t=0) = \phi_D \qquad [8]$$

for all pores, the inlet boundary conditions of current conservation,

$$\left.\frac{\partial\varphi_i}{\partial z_i}\right|_{z_i=0} = \frac{A_{s,i}}{A_i\ell_{s,i}}\varphi_i(z_i=0,t), \qquad [9a]$$

Table 1. Boundary conditions for the direct numerical simulations

Boundary	Equations
Reservoir-SDL interface	$\phi = 0$ $c_\pm = c_\infty$
Axis of symmetry of the SDL and the inlet pore Outer bounds of the SDL Dead ends of pores	$\hat{\mathbf{n}}\cdot\nabla\phi = 0$ $\hat{\mathbf{n}}\cdot\nabla c_\pm = 0$
Outer surfaces of the blocking pores	$\phi = \phi_D$ $\hat{\mathbf{n}}\cdot\nabla\mathbf{N}_\pm = 0$

for pores connected to SDLs, where the additional subscript *s* denotes properties of the SDL, and the no-flux boundary conditions

$$\left.\frac{\partial\varphi_i}{\partial z_i}\right|_{z_i=\ell_i} = 0 \qquad [9b]$$

for any dead ends of pores. More details about the initial and boundary conditions are provided in *SI Appendix*.

We solve this system of equations for a single junction with *n* dead-end pores analytically in *SI Appendix*. Though the analytical method is also applicable to general networks, it becomes more cumbersome. Therefore, we solve the equations for lattices numerically. The governing equations are discretized only in space by second-order central finite differences. Labeling the points by the superscript *j*, the *m* grid points in the *i*-th pore are $z_i^j = (j-1)\Delta z_i$ for $j = 1, \cdots, m$, where the mesh width is $\Delta z_i = \ell_i/(m-1)$. Furthermore, we introduce fictitious points z_i^0 and z_i^{m+1} defined by the same general formula as z_i^j, which are constrained by the central finite difference expressions of the boundary conditions, allowing the expression of these boundary conditions as differential equations (61). The grid functions $\varphi_i^0, \varphi_i^1, \cdots, \varphi_i^{m+1}$ consist of approximations of the electrochemical potential of charge at the grid points, $\varphi_i(z_i^j, t) \approx \varphi_i^j(t)$. In terms of this grid function, second derivatives in the axial coordinate are approximated in the inner points by

$$\left.\frac{\partial^2\varphi_i}{\partial z_i^2}\right|_{z_i=z_i^j} \approx \frac{\varphi_i^{j-1} - 2\varphi_i^j + \varphi_i^{j+1}}{(\Delta z_i)^2}, \quad j = 1, \cdots, m \qquad [10a]$$

and central differences are used for the first derivatives at the boundary points, namely

$$\left.\frac{\partial\varphi_i}{\partial z_i}\right|_{z_i=0} \approx \frac{\varphi_i^2 - \varphi_i^0}{2\Delta z_i} \qquad [10b]$$

and

$$\left.\frac{\partial\varphi_i}{\partial z_i}\right|_{z_i=\ell_i} \approx \frac{\varphi_i^{m+1} - \varphi_i^{m-1}}{2\Delta z_i}. \qquad [10c]$$

From current conservation and continuity of the effective electrochemical potential, for any pore *i* connected to a junction,

$$\frac{d\varphi_i^{j_i}}{dt} = 2\frac{\sum_{k\in\text{junction}} A_k\delta\varphi_k^{j_k}/\ell_k}{\sum_{k\in\text{junction}} \ell_k A_k/\mathcal{D}(\kappa_k)}, \qquad [11]$$

where j_i is the point of the *i*-th pore that is connected to the junction. $\delta\varphi_k^{j_k}$ is the difference between the effective potential of the neighbor and the boundary point. $\delta\varphi_k^{j_k} = \varphi_k^2 - \varphi_k^1$ if the $j_k = 1$ is the point of pore *k* connected to the junction, and $\delta\varphi_k^{j_k} = \varphi_k^m - \varphi_k^{m-1}$ if $j_k = m$.

The system of ordinary differential equations resulting from the discretization of Eq. **4** and the boundary conditions in Eqs. **5** and **9** couples the discretized

electrochemical potentials of charge of all pores. We solve it using ode15s, MATLAB's stiff differential equation solver, and providing upfront the sparsity pattern of the Jacobian matrix. A logarithmically spaced time span array in the interval $[10^{-6}, 2] \times (N_y - 1)^2$, where N_y is the number of inlet pores of the lattice, is input to ode15s to enforce a small initial step. We choose $m = 50$ grid points in each pore to achieve grid-size independence of the total current going into the networks (to within 1% of the current for $m = 100$) and retrieve the correct total network charge, known from the steady-state charge density $\bar{\rho}_i^* \to -1/\mathcal{D}_i^*$; see *SI Appendix*.

Pore Network Plots and Properties. DNS in Fig. 2 are performed with the parameters $c_\infty = 1$ mM, $\phi_D = 10$ mV, $\ell = \ell_1 = \ell_2 = \ell_3 = 1\,\mu$m, $D = 1.34 \times 10^{-9} m^2/s$ and $kT/e = 25.7$ mV. The inlet pore has a relative size (half-width by Debye length) $\kappa_1 = 4$ and is connected to the SDL with a Biot number $\mathrm{Bi}_1 = A_{s,1}/(A_1 \ell_{s,1}) = 2$.

All pore lattice network simulations performed in Figs. 3 and 4 and in *SI Appendix* used the transmission-line model in the limit $\mathrm{Bi}_i \to \infty$. Contour plots of the electrochemical potential of charge and the electric potential are respectively colored using viridis and plasma, perceptually uniform colormaps. The junctions, not resolved by the model, are delineated by white dashed squares and colored according to the arithmetic average of the properties on all sides. This is done to represent that current flows through the junctions as well. The pore sizes of the polydisperse lattices were drawn from pseudorandom samples of log-normal distributions using MATLAB's lognrnd routine, which takes as inputs the parameters μ and σ of the distribution, calculated based on the desired mean and variance.

The net charging time scale τ_{num} is numerically calculated in Figs. 3*B* and 4 and *SI Appendix* as the time required for the network to reach 70.18% of its steady-state charge divided by $(N_y - 1)^2$, where N_y is the number of nodes of the lattice in the direction normal to charging (or the number of inlets, such that square lattices where $N_x = N_y$ are the reference geometry for the horizontal diffusion-like charging). The division by the number of pores per side squared factors out the length of lattice, making square lattices of different numbers of pores per side comparable, and the percentage is chosen such that $\tau_{\mathrm{num}}^* = 4/(\pi^2 \mathcal{D})$ for monodisperse capillary bundles (33), where $\mathcal{D}^*$ is the dimensionless common effective diffusivity of the pores. On the other hand, the dimensionless extensive capacitance of a lattice is known based upon the dimensionless steady-state charge density $\bar{\rho}_i^* \to -1/\mathcal{D}_i^*$ as $t \to \infty$ to be $C^* = \sum_{i=1}^{N} (A_i^*/\mathcal{D}_i^*)$ for equal pore lengths. In the lattice plots of Fig. 4 and *SI Appendix*, where $N_x = N_y = N_\ell$, we normalize the extensive capacitance by the total pore volume of the fully connected monodisperse lattice with the same pore lengths and average relative sizes, $2\pi(N_\ell - 1)^2 \langle\kappa\rangle^2$ for cylindrical pores. Therefore, the capacitance per unit volume that we report is calculated as

$$C^* = \frac{\sum_{i=1}^{N} (\kappa_i^2/\mathcal{D}_i^*)}{2(N_\ell - 1)^2 \langle\kappa\rangle^2}, \qquad [12]$$

where $\langle\kappa\rangle$ is the average radius of the log-normal distribution. When multiplied by the porosity of the reference monodisperse configuration, Eq. **12** yields the dimensionless electrode volumetric capacitance, i.e., the dimensionless capacitance by the electrode volume.

The power density is simply calculated as the ratio of capacitance to charging time scale,

$$\mathcal{P}^* = \frac{C^*}{\tau_{\mathrm{num}}^*}. \qquad [13]$$

Data, Materials, and Software Availability. The methods required to reproduce the results in the paper are completely described in the paper and supporting information. The code used to produce the results and the data from the direct numerical simulations used for validation are available on Zenodo: 10.5281/zenodo.11133745 (62).

ACKNOWLEDGMENTS. We would like to acknowledge the helpful input provided by Gesse Roure, Nitish Govindarajan, Tiras Lin, Howard Stone, and Wilson Smith. We acknowledge that the simulations reported in this contribution were performed using the Princeton Research Computing resources at Princeton University which is a consortium of groups including the Princeton Institute for Computational Science and Engineering and the Princeton University Office of Information Technology's Research Computing department. A.G. thanks the NSF (CBET-2238412) CAREER award for financial support. F.H. thanks the Ryland Graduate Family Fellowship for financial assistance. P.J.Ż. would like to acknowledge the support of a project that has received funding from the European Union's Horizon 2020 research and innovation program under the Marie Skłodowska-Curie Grant Agreement No. 847413 and was part of an international cofinanced project founded from the program of the Minister of Science and Higher Education entitled "PMW" in the years 2020–2024; Agreement No. 5005/H2020-MSCA-COFUND/2019/2.

Author affiliations: [a]Department of Chemical and Biological Engineering, University of Colorado, Boulder, CO 80303; [b]Institute of Physical Chemistry, Polish Academy of Sciences, Warsaw 01-224, Poland; and [c]Department of Physics, Lancaster University, Lancaster LA1 4YB, United Kingdom

1. M. Z. Bazant, K. Thornton, A. Ajdari, Diffuse-charge dynamics in electrochemical systems. *Phys. Rev. E* **70**, 021506 (2004).
2. C. Ho *et al.*, Electrolytic transport through a synthetic nanometer-diameter pore. *Proc. Natl. Acad. Sci. U.S.A.* **102**, 10445–10450 (2005).
3. M. Muthukumar, C. Kong, Simulation of polymer translocation through protein channels. *Proc. Natl. Acad. Sci. U.S.A.* **103**, 5273–5278 (2006).
4. S. M. Davidson, M. B. Andersen, A. Mani, Chaotic induced-charge electro-osmosis. *Phys. Rev. Lett.* **112**, 128302 (2014).
5. L. Jubin, A. Poggioli, A. Siria, L. Bocquet, Dramatic pressure-sensitive ion conduction in conical nanopores. *Proc. Natl. Acad. Sci. U.S.A.* **115**, 4063–4068 (2018).
6. P. Simon, Y. Gogotsi, Materials for electrochemical capacitors. *Nat. Mater.* **7**, 845–854 (2008).
7. P. Simon, Y. Gogotsi, Perspectives for electrochemical capacitors and related devices. *Nat. Mater.* **19**, 1151–1163 (2020).
8. H. Sakaguchi, R. Baba, Charging dynamics of the electric double layer in porous media. *Phys. Rev. E* **76**, 011501 (2007).
9. P. Biesheuvel, M. Bazant, Nonlinear dynamics of capacitive charging and desalination by porous electrodes. *Phys. Rev. E* **81**, 031502 (2010).
10. M. Mirzadeh, F. Gibou, T. M. Squires, Enhanced charging kinetics of porous electrodes: Surface conduction as a short-circuit mechanism. *Phys. Rev. Lett.* **113**, 097701 (2014).
11. M. Schmuck, M. Z. Bazant, Homogenization of the Poisson–Nernst–Planck equations for ion transport in charged porous media. *SIAM J. Appl. Math.* **75**, 1369–1401 (2015).
12. Y. Jiang *et al.*, Large-surface-area activated carbon with high density by electrostatic densification for supercapacitor electrodes. *Carbon* **175**, 281–288 (2021).
13. T. Chu, S. Park, K. Fu, 3D printing-enabled advanced electrode architecture design. *Carbon Energy* **3**, 424–439 (2021).
14. S. Kondrat, G. Feng, F. Bresme, M. Urbakh, A. A. Kornyshev, Theory and simulations of ionic liquids in nanoconfinement. *Chem. Rev.* **123**, 6668–6715 (2023).
15. E. H. Lahrar, P. Simon, C. Merlet, Carbon–carbon supercapacitors: Beyond the average pore size or how electrolyte confinement and inaccessible pores affect the capacitance. *J. Chem. Phys.* **155**, 184703 (2021).
16. J. Wu, Understanding the electric double-layer structure, capacitance, and charging dynamics. *Chem. Rev.* **122**, 10821–10859 (2022).
17. M. S. Kilic, M. Z. Bazant, A. Ajdari, Steric effects in the dynamics of electrolytes at large applied voltages. I. Double-layer charging. *Phys. Rev. E* **75**, 021502 (2007).
18. M. S. Kilic, M. Z. Bazant, A. Ajdari, Steric effects in the dynamics of electrolytes at large applied voltages. II. Modified Poisson–Nernst–Planck equations. *Phys. Rev. E* **75**, 021503 (2007).
19. B. D. Storey, M. Z. Bazant, Effects of electrostatic correlations on electrokinetic phenomena. *Phys. Rev. E* **86**, 056303 (2012).
20. Z. Xu, M. Ma, P. Liu, Self-energy-modified Poisson–Nernst–Planck equations: WKB approximation and finite-difference approaches. *Phys. Rev. E* **90**, 013307 (2014).
21. A. Gupta, A. G. Rajan, E. A. Carter, H. A. Stone, Ionic layering and overcharging in electrical double layers in a Poisson–Boltzmann model. *Phys. Rev. Lett.* **125**, 188004 (2020).
22. J. P. de Souza, Z. A. Goodwin, M. McEldrew, A. A. Kornyshev, M. Z. Bazant, Interfacial layering in the electric double layer of ionic liquids. *Phys. Rev. Lett.* **125**, 116001 (2020).
23. S. Kondrat, P. Wu, R. Qiao, A. A. Kornyshev, Accelerating charging dynamics in subnanometre pores. *Nat. Mater.* **13**, 387–393 (2014).
24. R. J. Tomlin, T. Roy, T. L. Kirk, M. Marinescu, D. Gillespie, Impedance response of ionic liquids in long slit pores. *J. Electrochem. Soc.* **169**, 120513 (2022).
25. R. De Levie, On porous electrodes in electrolyte solutions: I. Capacitance effects. *Electrochim. Acta* **8**, 751–780 (1963).
26. R. De Levie, On porous electrodes in electrolyte solutions–IV. *Electrochim. Acta* **9**, 1231–1245 (1964).
27. J. M. Black, H. A. Andreas, Pore shape affects spontaneous charge redistribution in small pores. *J. Phys. Chem. C* **114**, 12030–12038 (2010).
28. J. Moškon, M. Gaberšček, Transmission line models for evaluation of impedance response of insertion battery electrodes and cells. *J. Power Sources Adv.* **7**, 100047 (2021).
29. S. Bi *et al.*, Molecular understanding of charge storage and charging dynamics in supercapacitors with MOF electrodes and ionic liquid electrolytes. *Nat. Mater.* **19**, 552–558 (2020).

30. L. Zeng *et al*., Modeling galvanostatic charge-discharge of nanoporous supercapacitors. *Nat. Comput. Sci.* **1**, 725–731 (2021).
31. M. Janssen, Transmission line circuit and equation for an electrolyte-filled pore of finite length. *Phys. Rev. Lett.* **126**, 136002 (2021).
32. A. Gupta, P. J. Zuk, H. A. Stone, Charging dynamics of overlapping double layers in a cylindrical nanopore. *Phys. Rev. Lett.* **125**, 076001 (2020).
33. F. Henrique, P. J. Zuk, A. Gupta, Charging dynamics of electrical double layers inside a cylindrical pore: Predicting the effects of arbitrary pore size. *Soft Matter* **18**, 198–213 (2022).
34. F. Henrique, P. J. Zuk, A. Gupta, Impact of asymmetries in valences and diffusivities on the transport of a binary electrolyte in a charged cylindrical pore. *Electrochim. Acta* **433**, 141220 (2022).
35. C. Lian, M. Janssen, H. Liu, R. van Roij, Blessing and curse: How a supercapacitor's large capacitance causes its slow charging. *Phys. Rev. Lett.* **124**, 076001 (2020).
36. G. Paasch, K. Micka, P. Gersdorf, Theory of the electrochemical impedance of macrohomogeneous porous electrodes. *Electrochim. Acta* **38**, 2653–2662 (1993).
37. R. B. Smith, M. Z. Bazant, Multiphase porous electrode theory. *J. Electrochem. Soc.* **164**, E3291 (2017).
38. J. Huang *et al*., Editors' choice-review-impedance response of porous electrodes: Theoretical framework, physical models and applications. *J. Electrochem. Soc.* **167**, 166503 (2020).
39. S. Alizadeh, M. Z. Bazant, A. Mani, Impact of network heterogeneity on electrokinetic transport in porous media. *J. Colloid Interface Sci.* **553**, 451–464 (2019).
40. P. Biesheuvel, Y. Fu, M. Z. Bazant, Diffuse charge and faradaic reactions in porous electrodes. *Phys. Rev. E* **83**, 061507 (2011).
41. C. K. Alexander, M. N. O. Sadiku, *Fundamentals of Electric Circuits* (McGraw-Hill, 2013).
42. W. M. Deen, *Analysis of Transport Phenomena* (Oxford University Press, New York, NY, 1998).
43. A. J. Bard, L. R. Faulkner, *Electrochemical Methods: Fundamentals and Applications* (Wiley, 2000).
44. P. Peters, R. Van Roij, M. Z. Bazant, P. Biesheuvel, Analysis of electrolyte transport through charged nanopores. *Phys. Rev. E* **93**, 053108 (2016).
45. S. Alizadeh, A. Mani, Multiscale model for electrokinetic transport in networks of pores. Part I: Model derivation. *Langmuir* **33**, 6205–6219 (2017).
46. J. S. Newman, C. W. Tobias, Theoretical analysis of current distribution in porous electrodes. *J. Electrochem. Soc.* **109**, 1183 (1962).
47. H. Tao, Z. Xu, C. Lian, R. van Roij, H. Liu, Charging dynamics in a laminate-electrode model for graphene-based supercapacitors. *AIChE J.* **69**, e18189 (2023).
48. V. Presser *et al*., The electrochemical flow capacitor: A new concept for rapid energy storage and recovery. *Adv. Energy Mater.* **2**, 895–902 (2012).
49. C. Zhang *et al*., Highly porous carbon spheres for electrochemical capacitors and capacitive flowable suspension electrodes. *Carbon* **77**, 155–164 (2014).
50. T. Mo *et al*., Horn-like pore entrance boosts charging dynamics and charge storage of nanoporous supercapacitors. *ACS Nano* **15**, 14974–14980 (2023).
51. C. Pedersen, T. Aslyamov, M. Janssen, Equivalent circuit and continuum modeling of the impedance of electrolyte-filled pores. *PRX Energy* **2**, 043006 (2023).
52. A. Gupta, H. A. Stone, Electrical double layers: Effects of asymmetry in electrolyte valence on steric effects, dielectric decrement, and ion–ion correlations. *Langmuir* **34**, 11971–11985 (2018).
53. N. Jarvey, F. Henrique, A. Gupta, Ion transport in an electrochemical cell: A theoretical framework to couple dynamics of double layers and redox reactions for multicomponent electrolyte solutions. *J. Electrochem. Soc.* **169**, 093506 (2022).
54. N. Jarvey, F. Henrique, A. Gupta, Asymmetric rectified electric and concentration fields in multicomponent electrolytes with surface reactions. *Soft Matter* **19**, 6032–6045 (2023).
55. K. Fu *et al*., Graphene oxide-based electrode inks for 3D-printed lithium-ion batteries. *Adv. Mater.* **28**, 2587–2594 (2016).
56. S. Fleischmann *et al*., Continuous transition from double-layer to faradaic charge storage in confined electrolytes. *Nat. Energy* **7**, 222–228 (2022).
57. R. Eymard, T. Gallouët, R. Herbin, Finite volume methods. *Handb. Numer. Anal.* **7**, 713–1018 (2000).
58. H. K. Versteeg, W. Malalasekera, *An Introduction to Computational Fluid Dynamics: The Finite Volume Method* (Pearson Education, 2007).
59. H. G. Weller, G. Tabor, H. Jasak, C. Fureby, A tensorial approach to computational continuum mechanics using object-oriented techniques. *Comput. Phys.* **12**, 620–631 (1998).
60. H. Jasak *et al*., "OpenFOAM: A C++ library for complex physics simulations" in *International Workshop on Coupled Methods in Numerical Dynamics* (IUC, Dubrovnik, Croatia, 2007), vol. 1000, pp. 1–20.
61. J. Crank, *The Mathematics of Diffusion* (Clarendon, Oxford, UK, 1975).
62. F. Henrique, P. J. Żuk, A. Gupta, A Network Model to Predict Ionic Transport in Porous Materials: Code. Zenodo. https://zenodo.org/records/11134482. Deposited 7 May 2024.